International Conference on Applied Energy 2019
Aug 12-15, 2019, Västerås, Sweden
Paper ID: 67

DESIGN, EXPERIMENT AND MODELLING OPTIMIZATION FOR A HIGH-TEMPERATURE AND MEDIUM-TEMPERATURE COUPLED TEG SYSTEM DRIVEN BY DIRECT COMBUSTION HEAT SOURCE

Shaowei Qing[1,2*], Wen Chen[1,2], Zhou Hu[1,2], Xiaolong Gou[1,2], Shengli Tang[1,2]

1 Key Laboratory of Low-grade Energy Utilization Technology and System, Chongqing University, Ministry of Education, Chongqing 400044, China;

2 Department of Energy and Power Engineering, Chongqing University, Chongqing 400044, China

ABSTRACT

A natural-gas-fired thermoelectric generation (TEG) system is an efficient way for simultaneously providing heat and electric power, and it can be used as a movable power system for field trips and a heat-power coordinated supply for residential homes. In this paper, a high-temperature and medium-temperature coupled TEG system driven by direct combustion heat source is proposed, and a new burner with baffle is designed to enhance the heat transfer between fired gas and the hot side of TEG. The optimal geometrical dimensions of the new burner are obtained by conducting a 2D model in ANSYS, which including combustion reactions, flow, and heat transfer in simplified TEGs. Comparative experiment results show that the inner-wall temperature of high-temperature TEG module averagely increases by 73K, and the power generation and conversion efficiency of the TEG system are improved by 42.48% and 3.38%, respectively. In order to further improve the performance of high-temperature TEG, the 2D model is developed by using an equivalent thermoelectric effects model of segmented high-temperature TEG, and its accuracy is verified by the experimental results. The influences of thermo-element length and number on TEG performance are revealed, and further improvement method, i.e. adding fins in the cold water jacket is proposed and verified.

Keywords: High-temperature and medium-temperature coupled TEG system; Burner; Geometric and cold side optimization

1. INTRODUCTION

Thermoelectric generation (TEG) is a novel and promising technology for energy harvest and utilization, which can convert heat into electric power directly based on the well-known thermoelectric (TE) effects [1]. It has many advantages such as all-solid energy conversion, no noise, no wear, no medium leakage, small size, light weight, easy to move, and long service life [2]. So far, a large number of studies have successfully applied the TEG technology to various heat sources. For example, in the field of solar energy utilization, TEG combined with micro-channel-heat-pipe, photovoltaic, water-heating systems can achieve more electric power and higher energy conversion efficiency [3-5]. In the field of metallurgical and transport industries, TEG technology has great application potential to harvest the large amount of waste heat from high-temperature slag [6], slag flushing water [7], and exhaust gas of engine [8-14]. In the field of sensor, TEG can be integrated as a power source for self-powered wearable monitor of human body [15, 16]. In the field of portable power generation, TEG combined with micro combustor can supply low-power electronic equipment [17]. In addition, arranging TEG around a macroscopic-scale burner can flexibly and conveniently provide heat and electric power simultaneously, and thus it can be used as a movable power system for field trips and a heat-power coordinated supply for residential homes.

For the combustion-driven TEG-based combined heating and power system, although it has obviously higher energy utilization efficiency than divided system,

Selection and peer-review under responsibility of the scientific committee of the 11th Int. Conf. on Applied Energy (ICAE2019).

the electric power generation by TEG is usually far smaller than heating supply power. Therefore, in order to enhance the adaptability of such a system, many researchers have devoted to improving TEG performance. Raman et al. designed a forced draft clean combustion cookstove, and achieved 4.5 W electric power and 44% overall efficiency [18]. Champier et al. showed that a 6 W electrical power production is possible from biomass cook stove [19]. Alptekin et al. designed a self-powered thermoelectric power supply system driven by fired-gas, and reached maximum output voltage and current of 35.96 V and 1.79 A respectively [20]. Bargielet al. showed that computational fluid dynamics (CFD) is a useful method for design and optimization of natural-gas-fired TEG [21]. Zhao et al. showed a 15% increment of output power by humidifying flue gas [22]. Ismail et al. coupled TEG with porous medium burner, and obtained 9.7 V total voltage which can be used for cell phone charging [23]. Qiu and Hayden proposed a natural-gas-fired combined heat and power system for residential home, in which the coupled annular TEG with heat-conducting fins on hot side can generate an electric power of several hundred Watts [24, 25].

Above literatures indicate that enhancing heat transfer at hot side and cold side of TEG with methods of force convection, extra heat-conducting fins, and new burner design can remarkably improve system efficiency. In addition, Gou et al. showed that cascaded TEG system can realize 21.56% efficiency increment in comparison with single-stage TEG system [26].

In this work, a natural-gas-fired high-temperature and medium-temperature coupled TEG system is proposed, in which a new type of burner with baffle is specially designed to enhance heat transfer between fired gas and the hot side of TEG. In the design stage, a 2D model which including combustion reactions and heat transfer in simplified TEGs (i.e. the two TEGs are simplified as homogeneous heat conductors) is built to realize the optimal geometric dimensions of the new burner. Comparative experiment results show that the new burner design can improve the output power and conversion efficiency of the TEG system significantly. Moreover, in the TEG-system-optimization stage, a 2D multi-physics coupled model which including 2D combustion reactions in the new burner and 1D multi-physical TE effects of segmented high-temperature TEG module is established and verified by the experimental results to further improve TEG performance. Then, the effects of TE element length and number on output power are revealed. Finally, further optimization method, i.e. adding fins in the cold water jacket is assessed and verified.

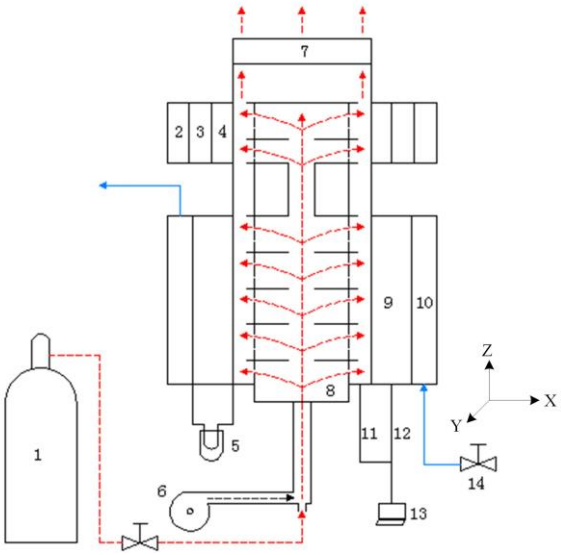

1. Gas bottle. 2. Cooling fin. 3. Medium-temperature TEG module. 4. Pedestal. 5. Load. 6. Fan. 7. Exhaust device. 8. Burner. 9. High-temperature TEG module. 10. Heat sink. 11. Temperature signal. 12. Current signal. 13. Computer. 14. Valve.

Fig.1 Schematic diagram of annular high-temperature

2. HIGH-TEMPERATURE AND MEDIUM-TEMPERATURE COUPLED TEG SYSTEM: A NEW BURNER DESIGN

2.1 High-temperature and medium-temperature coupled TEG system

The schematic diagram of annular high-temperature and medium-temperature coupled TEG system driven by direct combustion heat source is shown in Fig. 1. This TEG system consists of a natural gas burner, cooling device, data acquisition device and high-temperature and medium-temperature TEGs. The combustion of mixed gas occurs in the burner, producing high

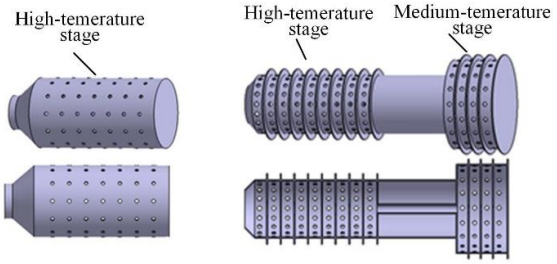

(a) The old burner in single-stage high-temperature TEG (b) The new burner in high- and medium-temperature coupled TEG

Fig.2 Comparison of different burner structures, (a) the annular multi-hole flame-shielding burner, (b) the annular multi-hole two-stage flame-shielding burner with baffle

temperature flue gas. The inner walls of the two TEGs directly contact with the flue gas. At the same time, the high-temperature TEG uses cooling water for heat dissipation, while the medium-temperature TEG uses natural cooling mode.

The high-temperature TEG module is composed of 325 pairs of p- and n-type thermocouples with a diameter of 10mm and a length of 5.5mm arranged in series. The material of p-type semiconductor is PbSnTe, and the material of n-type semiconductor is PbTe/PbSnTe. The geometric dimensions of the annular high-temperature TEG are: inner wall diameter 150 mm, outer wall diameter 220 mm, thickness 35mm and height 248 mm.

The medium-temperature TEG is selected to match the temperature of flue gas, and four commercial modules, i.e. TEHP1-24156-1.2 (40 mm×40 mm×2 mm) made by BiTe semiconductor are chosen.

Fig.2 (a) shows the 3D structure of the old burner for single-stage high-temperature TEG system, while Fig.2 (b) shows the new designed two-stage burner for high-temperature and medium-temperature coupled TEG system. The new type burner of annular multi-hole flame shield with baffle is designed to enhance heat transfer between inner wall and flue gas, and it is divided into high-temperature part and medium-temperature part with a connective circular pipe in the middle.

2.2 Parametric optimization design of the new burner: A 2D model of combustion, flow and heat transfer

As shown in Fig. 1, the high-temperature fired flue gas is divided into two parts. One part (the main part) goes to heat the inner wall of high-temperature TEG at first and then to heat the medium-temperature TEG, while another part goes into the medium-temperature stage of the new burner directly through the central annular catheter. Obviously, in order to strengthen the heat transfer between the flue gas and the inner walls of the two TEGs, the sizes of baffle, side round hole, central annular catheter and hole should be optimally desgned.

For this purpose, a 2D computational fluid dynamics (CFD) model which contains combustion, flow and heat transfer in the two TEGs is established. In particular, the two TEGs are simplified as homogeneous heat conductors to accelerate the multi-parameters design process of the new burner, since we only concern the temperature near the inner wall of TEG. In the model, Gambit pre-processor is used to mesh the TEG system with Quad unstructured grid, standard $k-\varepsilon$ model is selected for the turbulence model of the system, the finite rate/eddy dissipation model is selected for combustion model, methane and oxygen are set at the inlet with a ratio of 1:1.3. Based on necessary grid-independence verification, a grid number of 362272 is chosen to reconcile enough simulation accuracy and speed.

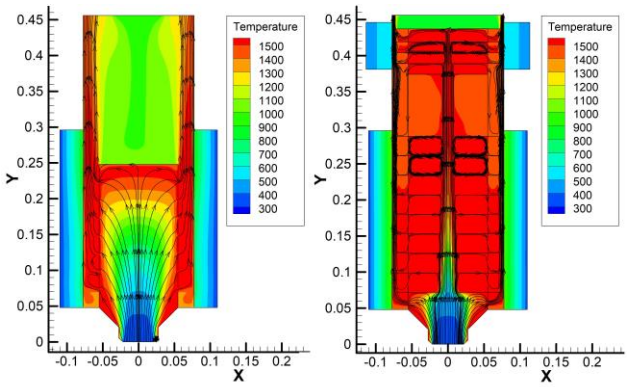

Fig.3 The temperature contour and streamline diagrams of (a) single-stage high-temperature TEG system and (b) high-temperature and medium-temperature coupled TEG system

With extensive calculations, the optimal geometric dimensions of the new burner are obtained. As shown in Fig. 3, in comparison with the temperature contour and streamline diagrams of the single-stage TEG system, one can see that the flue gas temperature and the temperature near the inner wall of high-temperature and medium-temperature coupled TEG system are significantly increased and become more uniform along Z direction because of the added ring baffle. Therefore, it is expected that the new burner design can effectively improve TEG performance.

3. CONTRAST EXPERIMENTS

Contrast experiments for the single-stage high-temperature TEG system and high-temperature and medium-temperature coupled TEG system are built and tested. The whole experimental device is composed of combustion system, cooling system, exhaust system, TEG module system, data acquisition system and safety monitoring system, as shown in Fig. 4. The data of temperature, natural gas flow, flue gas flow, cooling water flow, voltage and current generated by the TEGs and electric power consumed by the fan are collected in experiment.

The burner of single-stage high-temperature TEG system is made of graphital/ceramic composites, while the new two-stage burner is made of 310S alloy

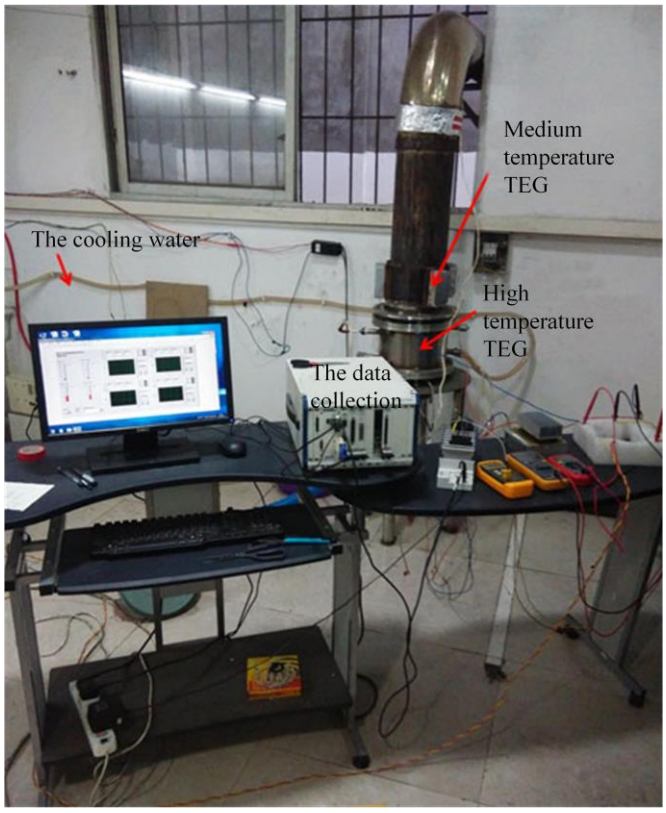

Fig.4 Experimental facility of the high-temperature and medium-temperature coupled TEG system

stainless steel. The inner-wall temperature of TEG is measured by S-type platinum-rhodium thermocouple with an error range of ±1 °C.

The hot side temperature of TEG is a key parameter in TEG system. As for the inner-wall temperature distributions in the high-temperature TEG module of the two TEG systems shown in Fig. 5, the inner-wall temperature in high-temperature TEG module of the coupled TEG system is much higher than that of single-stage TEG system. The temperature of inner wall in the high-temperature module of the coupled TEG system decreases first and then increases along Z axis. The reason is that the gas burning core locates near the bottom of the high-temperature TEG module (see Fig. 3(b)), releasing a large amount of heat and resulting in large temperature fluctuations there. Because of the enhanced turbulence of flue gas by the baffle of flame shield, the flow velocity of flue gas increases, and the convective heat transfer between flue gas and wall surface increases too. Therefore, the inner wall temperature of the new coupled TEG system is about averagely 73K higher than that of the single-stage TEG system. Moreover, due to appropriate split-flow design of flue gas in the new burner (see Fig. 1, Fig. 2(b) and Fig. 3(b)), the measured inner-wall temperature in the medium-temperature TEG module become approximately uniformly distribution along Z axis with the temperature around 489-495K.

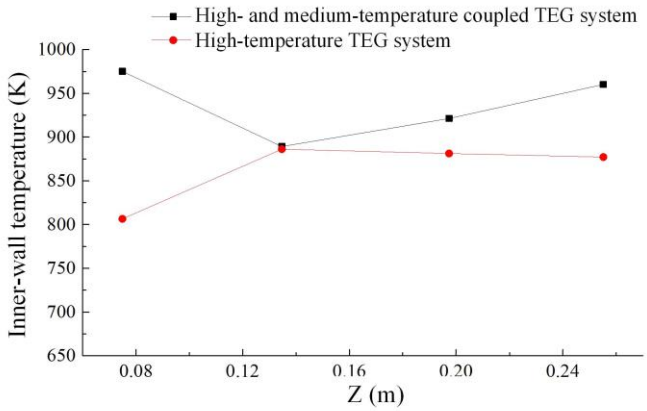

Fig.5 Contrast experiment results of temperature along inner wall of the two different TEG systems

Table 1 presents experimental results for the two systems. Compared with the single-stage TEG system, the performance of the new TEG system is significantly improved, e.g. (1) the net output electric power of the new TEG system reaches 393.96W, with 42.48% power increment and 3.38% system efficiency increment; (2) the output power of high-temperature TEG increases by 43.84W, with a growth rate of 14.3%. Below we are going to optimize the high-temperature TEG module by a developed 2D multi-physical field coupled model.

Table 1 Experimental results for the two TEG systems

TEG system	Fuel input ($m^3 \cdot h^{-1}$)	High-temperature TE module power (W)	Middle-temperature TE module power (W)	Fan power consumption (W)	Net system power (W)	System efficiency (%)
Single-stage high temperature TEG system	0.17	306.6	0	80.1	226.6	4.58
High-temperature and medium-temperature coupled TEG system	0.17	350.44	136.19	92.67	393.96	7.96

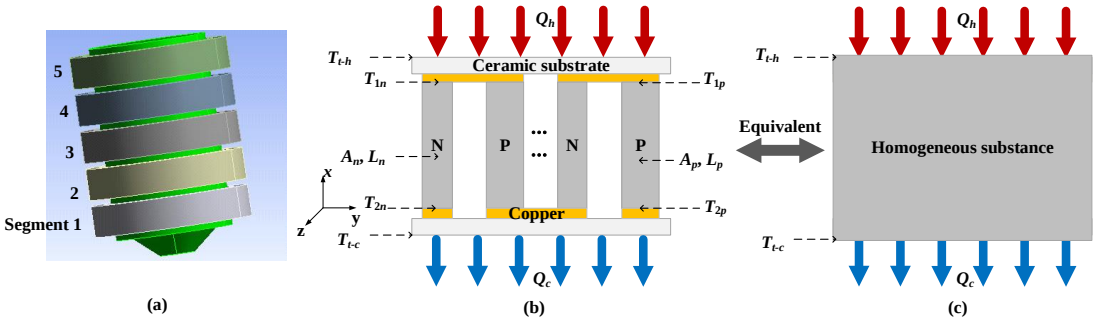

Fig.6 (a) Five segmented high-temperature TEG module for high-temperature TEG, (b) physical model for each segment, and (c) equivalent homogeneous substance model

4. HIGH-TEMPERATURE TEG MODULE OPTIMIZATION: A 2D MULTI-PHYSICAL FIELD COUPLED MODEL OF COMBUSTION, FLOW, AND TE EFFECTS OF SEGMENTED TEG

4.1 Modelling

In Section 2.2, a 2D CFD model with simplified TEGs was established to optimize the geometric dimensions of burner. Here, the 2D CFD model is further developed by coupling with TE effects to accurately predict the performance of high-temperature TEG, by referring to former coupling methodologies [27, 28]. For this purpose, the high-temperature TEG is divided into five modules which are connected in series, as shown in Fig. 6(a). For each segmented module, it is very complicated to establish 2D models for each p- or n-type TE element. Therefore, each segmented module is treated by equivalent simplification, as shown in Fig. 6(b) and 6(c).

4.1.1 Equivalence rules and coupled calculation process for each segmented module

According to the principle of energy conservation, each segmented module is equivalent to a uniform substance with radial thickness d, circumferential area A and equivalent thermal conductivity $k_{uniformity}$, as shown in Fig. 6(b) and 6(c). The specific equivalence rules are as follows:

(1) The average temperature ($T_{t\text{-}h}$, $T_{t\text{-}c}$) and heat flow (Q_h, Q_c) at hot and cold sides remain same before and after the equivalence.

(2) Q_c is the heat flow transferred to the cold source by means of heat conduction, so the equivalent thermal conductivity of the model is

$$k_{uniformity} = Q_c\, d / (A \Delta T). \tag{1}$$

(3) Due to $Q_h > Q_c$, there is an endothermic internal heat source in the equivalent substrate, namely

$$Q_{source} = Q_c - Q_h. \tag{2}$$

The coupling calculation process is shown in Fig. 7. The 2D CFD model gives two important quantities, i.e. the hot-side ($T_{t\text{-}h}$) and cold-side ($T_{t\text{-}c}$) average temperatures to the 1D TE effects coupling model. Then, Q_h and Q_c are calculated by the 1D coupling analytical model, and $k_{uniformity}$ and Q_{source} will be changed in the 2D CFD model.

4.1.2 Performance calculation of the segmented high-temperature TEG module

The output performance of the high-temperature TEG is calculated based on the 1D analytical Model of Ref. [29], in which the temperature-dependent material characteristics are considered.

The schematic diagram of each segmented module is shown in Fig. 6(b). Temperatures at hot side of the p-type and n-type TE elements (T_{1p}, T_{1n}) and at cold side of the elements (T_{2p}, T_{2n}) are not same for p- and n-type elements due to difference in temperature-dependent material properties such as Seebeck coefficient (α_p, α_n), electrical resistivity (ρ_p, ρ_n) and thermal

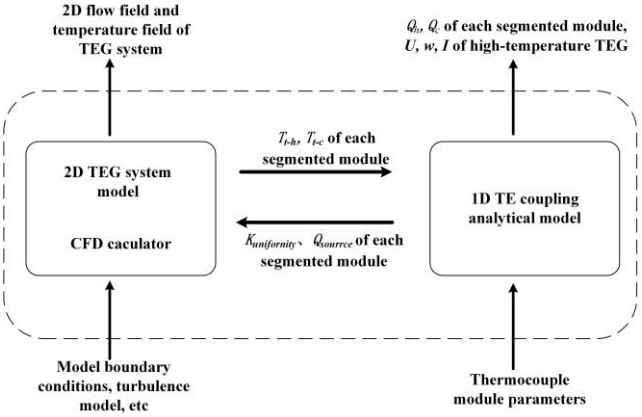

Fig.7 The coupling process diagram between the 2D CFD model and 1D analytical model for high-temperature TEG

conductivity (k_p , k_n). A_p , A_n and L_p , L_n are footprint areas and lengths for p- and n-type elements.

For each segmented module, the average Seebeck coefficient of the uni-couple and total electric voltage are:

$$\begin{aligned}\bar{\alpha}_i &= \bar{\alpha}_p - \bar{\alpha}_n \\ &= \frac{1}{T_{1p}-T_{2p}}\int_{T_{2p}}^{T_{1p}} \alpha_p \mathrm{d}T_p - \frac{1}{T_{1n}-T_{2n}}\int_{T_{2n}}^{T_{1n}} \alpha_n \mathrm{d}T_n ,\end{aligned} \tag{3a}$$

$$U_i = N_{uc}\left[\bar{\alpha}_p\left(T_{1p}-T_{2p}\right)-\bar{\alpha}_n\left(T_{1n}-T_{2n}\right)\right], \tag{3b}$$

where, $\bar{\alpha}_p$ and $\bar{\alpha}_n$ are, respectively, the average Seebeck coefficient of p- and n-type TE elements, N_{uc} is the uni-couple number of each segmented module, *i*=1, 2, … , 5.

The temperature dependent electrical resistance and thermal conductance of the p- and n-type TE elements are:

$$R_{p,n} = \int_0^{L_{p,n}} \frac{\rho_{p,n}\left(T_{p,n}(x)\right)}{A_{p,n}}\mathrm{d}x , \tag{4a}$$

$$K_{p,n} = \frac{1}{\int_0^{L_{p,n}} \mathrm{d}x \Big/ \left[k_{p,n}\left(T(x)\right)A_{p,n}\right]} . \tag{4b}$$

Based on the three-dimensional numerical results, the temperature through TE elements approximately obeys linear distribution [30]. Therefore, with the assumption of linear temperature distribution along TE elements, Eqs. (4a) and (4b) become:

$$R_{p,n} = \frac{L_{p,n}}{A_{p,n}}\frac{1}{T_{1p,n}-T_{2p,n}}\int_{T_{2p,n}}^{T_{1p,n}} \rho_{p,n}\mathrm{d}T = \frac{L_{p,n}}{A_{p,n}}\bar{\rho}_{p,n} , \tag{5a}$$

$$K_{p,n} = \frac{A_{p,n}}{L_{p,n}}\frac{1}{\frac{1}{T_{1p,n}-T_{2p,n}}\int_{T_{2p,n}}^{T_{1p,n}}\frac{1}{k_{p,n}}\mathrm{d}T} = \frac{A_{p,n}}{L_{p,n}}\frac{1}{\bar{r}_{p,n}} , \tag{5b}$$

where, $\bar{\rho}_{p,n}$ and $\bar{r}_{p,n}$ are the average electrical resistivity (Ωm) and average thermal resistivity (mK/W) of p- and n-type TE elements respectively. Therefore, the total internal resistance for each segmented module is $R_i = N_{uc}\left(R_p + R_n\right)$.

Consequently, circuit current of the high-temperature TEG is

$$I = \sum_{i=1}^{5} U_i \Big/ \left(R_L + \sum_{i=1}^{5} R_i\right), \tag{6}$$

and the output power is:

$$w = I^2 R_L , \tag{7}$$

where, R_L is load resistance.

Based on Ref. [29], T_{1p} is very close to T_{1n}, and T_{2p} is very close to T_{2n}. For this reason, in the 2D CFD model, the ceramic substrates in Fig. 6(b) and the inner and outer walls are simulated as annular cylinders. Therefore, in the 1D analytical Model, the temperature T_{1p} = T_{1n} =$T_{t\text{-}h}$, T_{2p} = T_{2n} =$T_{t\text{-}c}$. Once the temperatures $T_{t\text{-}h}$ and $T_{t\text{-}c}$ are given by the 2D CFD model, Eqs. (3), (5), (6) and (7) can be calculated, and thus the bilateral heat flux Q_h and Q_c as follows:

$$Q_h = N_{uc}\begin{bmatrix}\bar{\alpha}_i I T_{t-h} + (K_p + K_n)(T_{t-h} - T_{t-c}) \\ -I^2(R_p + R_n)/2\end{bmatrix}, \tag{8a}$$

$$Q_c = N_{uc}\begin{bmatrix}\bar{\alpha}_i I T_{t-c} + (K_p + K_n)(T_{t-h} - T_{t-c}) \\ +I^2(R_p + R_n)/2\end{bmatrix}. \tag{8b}$$

4.1.3 Cold source treatment of the segmented high-temperature module

The heat transfer coefficient of cold source h_c is calculated by convective heat transfer equation [31]:

$$Nu = 0.664\,\mathrm{Re}^{1/2}\,\mathrm{Pr}^{1/3},$$

where $Nu = h_c l/\lambda$, $\mathrm{Re} = ul/\nu$ and Pr are

Table 2 Temperature-dependent TE characteristics of P-type [32] and n-type [33] TE materials

TE parameters	Fitting formulars
Seebeck coefficient (V/K)	$\alpha_p = -2\times10^{-12}T^3 + 2.332\times10^{-9}T^2 - 5.88578\times10^{-7}T + 8.617\times10^{-5}$
	$\alpha_n = 1\times10^{-12}T^3 - 7.91\times10^{-10}T^2 - 4.5855\times10^{-8}T - 2.9121469\times10^{-5}$
Electrical conductivity (Ωm)	$\rho_p = 1/\left(-0.00075643T^3 + 2.08868T^2 - 1887.5052T + 585859.2097\right)$
	$\rho_n = 1/\left(-0.00085655T^3 + 2.00758T^2 - 1692.6528T + 535253.6813\right)$
Thermal conductivity (W/m/K)	$k_p = -2\times10^{-9}T^3 + 1.0442\times10^{-5}T^3 - 0.0126297T + 5.509085655$
	$k_n = -1\times10^{-9}T^3 + 8.148\times10^{-6}T^2 - 0.010582T + 4.769554$

characteristic numbers of convection heat transfer between the cold water and the cold side of high-temperature TEG. Characteristic length l is the height of high-temperature TEG. In the experiment and simulation, the cooling water flow and temperature are 12.5 L/min and 60 ℃. According to calculation, h_c=235 W/m^{2}K.

4.2 Model validation

In order to validate the accuracy of the 2D multi-physics field coupled model, the temperature-dependent TE characteristics of 2% Na doped $Pb_{0.99}Mg_{0.01}Se_{0.2}Te_{0.08}$ (P-type material) [32] and $Pb_{0.995}Sn_{0.005}Te_{0.982}Se_{0.15}I_{0.003}$ (n-type material) [33] are implemented. The fitting functions of the two TE materials are shown in Table 2.

The calculated output power 353 W is very close to the measured value 350.44 W, but the simulated inner wall temperature distribution is obviously bigger than that of experimental results, as shown in Fig. 8. Potential reasons for this difference are: (1) in simulation, the fuel is assumed as completed combustion, and the contact thermal and electric resistances are neglected; (2) in experiments, the platinum-rhodium thermocouples are fixed at the inner wall of high-temperature TEG by solid glue, which introducing extra thermal resistance; (3) the characteristics of TE materials in simulation aren't exactly the same with experimental TEG. Even so, the simulated temperature distribution in Fig. 8 presents a similar variety trend with measured distribution. Therefore, based on above results and analysis, the developed 2D multi-physical field coupled model can be a useful and accuracy tool for performance prediction and parametric optimization of TEG.

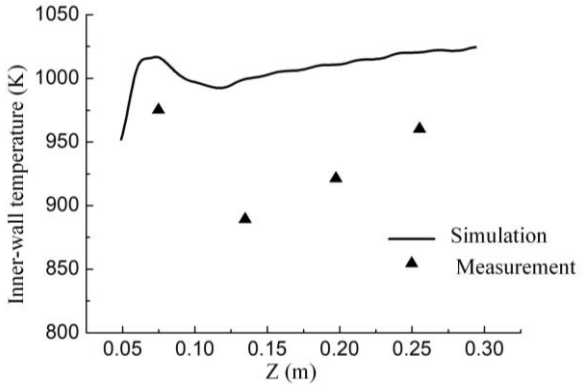

Fig.8 Inner-wall temperature distribution of high-temperature TEG for high- and medium-temperature coupled TEG system

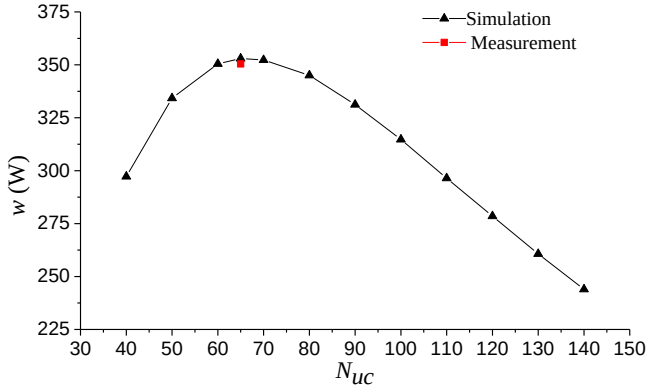

Fig.9 Effect of uni-couple number N_{uc} on output power w

4.3 Parametric Optimization and Discussion

4.3.1 Output power versus number of thermocouples

Output power of the high-temperature TEG versus the number of thermocouples is presented in Fig. 9. It shows that there is an optimum N_{uc} for the maximum output power. The maximum output power is 353 W with N_{uc}=65 (for each segmented high-temperature TEG module). The optimal N_{uc} and the corresponding maximum output power are very close to the

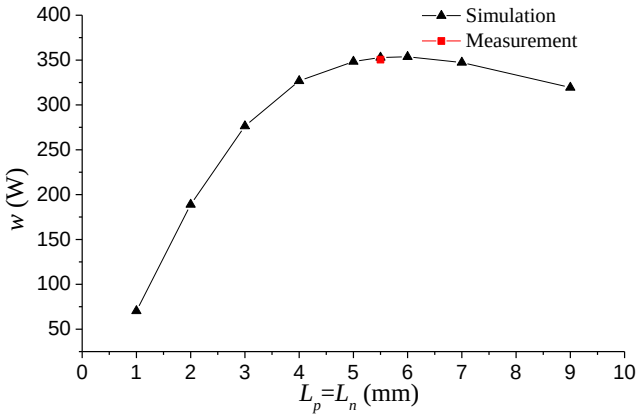

Fig.10 Effect of TE element length on output power

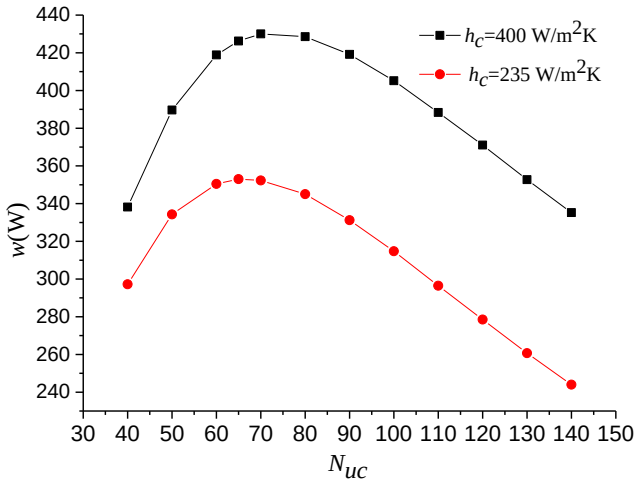

Fig.11 Output power w versus N_{uc} for cases of h_c=235 and 400 W/m^{2}K

experimental TEG module geometric parameter and corresponding experiment result shown in table 1.

4.3.2 Output power versus TE element length

The variation in output power for different lengths of thermocouples is presented in Fig. 10. It shows that there is an optimum L_p and L_n, for which the output power is maximum. The maximum output power is 353.68 W with optimal length L_p=L_n=6 mm. The optimal TE length (L_p and L_n) and the corresponding maximum output power are very close to the experimental TE module geometric parameter and corresponding experiment result shown in table 1.

4.3.3 Optimization of cold-side heat sink

In order to assess the effect of cold water jacket (i.e. h_c) on the performance of TEG, the output power versus uni-couple number for cases of h_c=235 and 400 W/m^{2}K are shown in Fig. 11. The maximum output power can be increased by 77.3 W, if we add fins in the water jacket which can potentially make h_c reach 400 W/m^{2}K. Therefore, adding extra fins in the cold water jacket can significantly improve the performance of high-temperature TEG.

5. CONCLUSIONS

In this paper, a high-temperature and medium-temperature coupled TEG system with a new burner design is proposed. A 2D CFD model including combustion reactions, flow, and heat transfer in the two simplified TEGs is built to optimize the detailed size of burner, and it is shown that the new designed burner with baffle can significantly enhance the heat transfer between fired flue gas and the hot side of TEG.

Comparative experiment results between the single-stage high-temperature TEG system and the coupled TEG system show that: (1) the inner-wall temperature of high-temperature TEG module averagely increases by 73K, and the output power of high-temperature TEG increases by 43.84W, with a growth rate of 14.3%; (2) the power generation and conversion efficiency of the coupled TEG system are improved by 42.48% and 3.38%, respectively.

To further optimize the high-temperature TEG module, a 2D multi-physics field coupled model which including 2D combustion reactions in the new burner and 1D multi-physical TE effects of segmented high-temperature TEG module is established and verified by the experimental results, and the effects of TE element length and number on output power are revealed. In addition, further optimization method, i.e. adding fins in the cold water jacket is assessed and verified.

ACKNOWLEDGEMENT

This work was supported in part by the National Natural Science Foundation of China under Grant 11605018 and Grant 51776023.

REFERENCE

[1]DiSalvo FJ. Thermoelectric cooling and power generation. Science 1999;285:703–6.

[2]Champer D. Thermoelectric generators: A review of applications. Energy Convers Manage 2017;140:167–81.

[3]Li GQ, Zhang G, He W, Ji J, Lv S, Chen X, et al. Performance analysis on a solar concentrating thermoelectric generator using the micro-channel heat pipe array. Energy Convers Manage 2016;112:191–8.

[4]Rezania A and Rosendahl LA. Feasibility and parametric evaluation of hybrid concentrated photovoltaic-thermoelectric system, Appl Energy 2017;187: 380–9.

[5]Hazama H, Masuoka Y et al. Cylindrical thermoelectric generator with water heating system for high solar energy conversion efficiency. Appl Energy 2018; 226: 381–8.

[6]Barati M, Esfahani S, Utigard TA. Energy recovery from high temperature slags. Energy 2011;36:5440–9.

[7]Meng FK, Chen LG, Sun FR, Yang B. Thermoelectric power generation driven by blast furnace slag flushing water. Energy 2014;66:965–72.

[8]Fernández-Yañez P, Armas O, Capetillo A, Martínez-Martínez S. Thermal analysis of a thermoelectric generator for light-duty diesel engines. Appl Energy 2018;226:690–702.

[9]Zhao Y, Wang S, Ge M, Liang Z, Liang Y, Li Y. Performance analysis of automobile exhaust thermoelectric generator system with media fluid. Energy Convers Manage 2018;171:427–37.

[10]Shu G, Ma X, Tian H, Yang H, Chen T, Li X. Configuration optimization of the segmented modules in an exhaust-based thermoelectric generator for engine waste heat recovery. Energy 2018;160:612–24.

[11]He W, Wang S. Thermoelectric performance optimization when considering engine power loss caused by back pressure applied to engine exhaust waste heat recovery. Energy 2017; 133: 584–592.

[12]Li B, Huang K, Yan Y, Li Y, Twaha S, Zhu J. Heat transfer enhancement of a modularised thermoelectric power generator for passenger vehicles. Appl Energy 2017;205:868–79.

[13] Kousksou T, Bedecarrats J-P, Champier D, Pignolet P, Brillet C. Numerical study of thermoelectric power

generation for an helicopter conical nozzle. J Power Sources 2011;196:4026–32.
[14]Kristiansen N, Snyder G, Nielsen H, Rosendahl L. Waste heat recovery from a marine waste incinerator using a thermoelectric generator. J Electron Mater 2012;41:1024–9.
[15]Kim CS, Lee GS, Choi H, Kim YJ, Yang HM, Lim SH, Lee SG, Cho BJ. Structural design of a flexible thermoelectric power generator for wearable applications. Appl Energy 2018;218:131–8.
[16]Qing S, Rezania A, Rosendahl LA, Gou X. Characteristics and parametric analysis of a novel flexible ink-based thermoelectric generator for human body sensor. Energy Convers Manage 2018;156:655–65.
[17]Fanciulli C, Abedia H, Merotto L, Dondè R, Iuliis SD, Passaretti F. Portable thermoelectric power generation based on catalytic combustor for low power electronic equipment. Appl Energy 2018;215:300–8.
[18]Raman P, Ram NK, Gupta R. Development, design and performance analysis of a forced draft clean combustion cookstove powered by a thermos electric generator with multi-utility options. Energy 2014;69:813–25.
[19]Champier D, Bedecarrats JP, Rivaletto M, Strub F. Thermoelectric power generation from biomass cook stoves. Energy 2010;35:935–42.
[20]Alptekin M, Calisir T, Baskaya S. Design and experimental investigation of a thermoelectric self-powered heating system. Energy Convers Manage 2017; 146:244–252.
[21]Bargiel P, Kostowski W, Klimanek A, Górny K. Design and optimization of a natural gas-fired thermoelectric generator by computational fluid dynamics modeling. Energy Convers Manage 2017;149:1037–1047.
[22]Zhao Y, Wang S, Ge M, Li Y, Liang Z. Analysis of thermoelectric generation characteristics of flue gas waste heat from natural gas boiler. Energy Convers Manage 2017;148:820–829.
[23]Ismail AK, Abdullah MZ, Zubair M, Ahmad ZA, Jamaludin AR, Mustafa KF, Abdullah MN. Application of porous medium burner with micro cogeneration System. Energy 2013;50:131–42.
[24]Qiu K, Hayden ACS. Development of a thermoelectric self-powered residential heating system. J Power Sources 2008;180:884–9.
[25]Qiu K, Hayden ACS. A Natural-Gas-Fired Thermoelectric Power Generation System. J Electron Mater 2009;38:1315–9.
[26]Shen R, Gou X, Xu H, Qiu K. Dynamic performance analysis of a cascaded thermoelectric generator. Appl Energy 2017;203:808–15.
[27]Högblom O and Andersson R. A simulation framework for prediction of thermoelectric generator system performance. Appl Energy 2016;180:472–482.
[28]Montecucco A, Siviter J, Knox AR. The effect of temperature mismatch on thermoelectric generators electrically connected in series and parallel. Appl Energy 2014;123:47–54.
[29]Qing S, Rezania A, Rosendahl LA, Gou X. An Analytical Model for Performance Optimization of Thermoelectric Generator With Temperature Dependent Materials. IEEE Access 2018;6:60852–61.
[30]Meng JH, Zhang XX, and Wang XD. Characteristics analysis and parametric study of a thermoelectric generator by considering variable material properties and heat losses. Int J Heat Mass Transf 2015;80:227–35.
[31]Yang S, Tao W. Heat Transfer. 4th ed. Beijing: Higher Education Press; 2006.
[32]Fu T, Yue X, Wu H, et al. Enhanced thermoelectric performance of PbTe bulk materials with figure of merit zT>2 by multi-functional alloying. J Materiomics 2016;2:141–9.
[33]Xiao Y, Li W, Chang C, Chen Y, Huang L, He J, Zhao LD. Synergistically optimizing thermoelectric transport properties of n-type PbTe via Se and Sn co-alloying. J Alloy Compd 2017;724:208–21.